journal

J. Am. Ceram. Soc., **80** [8] 2061–73 (1997)

Micromechanics of Failure Waves in Glass: I, Experiments

Horacio D. Espinosa* and Yueping Xu

School of Aeronautics and Astronautics, Purdue University, West Lafayette, Indiana 47907–1282

Natchater S. Brar

University of Dayton Research Institute, Dayton, Ohio 45469

Plate and bar impact experiments were performed on glass to investigate the mechanisms responsible for recently observed failure waves. In the present work we report observations showing that the so-called failure wave is actually a propagating boundary of damaged material. It initiates at the specimen surface, without appreciable incubation time, and propagates to its interior. In-material gauge measurements show that the spall strength and shear resistance of the material are drastically reduced behind the failure wave front. The shear resistance interferometrically measured in pressure-shear experiments is in agreement with the in-material gauge records. Normal stress measurements performed close to the impact surface show a progressive reduction in normal stress behind the failure wave. This feature suggests that the inelastic process responsible for the reduction in shear strength has well-defined kinetics. Recovery experiments performed on confined soda–lime glass rods reveal extensive material fragmentation. Microscopy studies performed on fracture surfaces show features commonly seen in glass fractured under tensile loading. Post-test X-ray experiments reveal that the material retains its amorphous structure. Two interpretations of the failure process, consistent with the above features, are discussed. The first mechanism is the initiation of microcracks, at the glass surfaces being subjected to compressive tractions, which propagate along surfaces of maximum shear to its interior. Another mechanism, based on the inhomogeneous nature of plastic flow in amorphous materials, is the initiation of shear-induced flow surfaces at the impact plane which are punched into the bulk of the material. In the latest, microcracks nucleated at the intersection of these shear flow surfaces are believed to be responsible for the dramatic reduction in spall strength behind the failure wave. The experimental observations herein presented are especially suitable for the formulation and examination of constitutive models describing damage evolution behind the so-called failure waves.

I. Introduction

THE response of different glasses (soda–lime, Pyrex, borosilicates, aluminosilicates, and fused quartz) to dynamic loading and unloading has been the subject of intense research in the last decade. A very complex material behavior emerged from these studies that has been explained in terms of a variety of inelastic mechanisms, namely, permanent densification, phase transformation, and cracking under compression. In the literature, the Hugoniot elastic limit (HEL) is defined as a measure of the dynamic stress required to initiate material inelasticity. In this paper we define the HEL as the stress level for which bulk glass undergoes permanent densification.

Cagnoux and Longy[1] have found that the spall strength of Pyrex (HEL 7.5 GPa) increases from about 1.2 to 2.3 GPa when the peak shock stress is varied from 3 to 5 GPa. Kanel *et al.*[2] have reported that the spall strength of K-8 glass (HEL 7.5–8 GPa) is about 3 ± 0.1 GPa for shock stresses up to 20 GPa (well above HEL). On the other hand, Rosenberg *et al.*[3] have found that the spall strength of soda–lime glass is about 3.8 GPa for shock levels below the HEL (6.4 GPa) while above the HEL the spall strength is negligible. These conflicting results were rationalized by invoking the existence of failure waves. Kanel *et al.*[2] were the first to report the propagation of failure waves behind the elastic and densification wave fronts in glass. They found that this wave propagates at about 1.5–2 mm/μs in shock-loaded K-19 glass (similar to soda–lime glass) plates and represents total failure of the specimen.

More recently, Brar and Bless[4] performed two types of normal impact experiments, wave interaction experiments and spall experiments, in order to confirm the existence of failure waves in glass. In the first type, a release wave that originates at the back of the target plate interacts with the advancing failure wave. In this experiment, a recompression was observed in the longitudinal stress history, similar to the increase in free surface particle velocity detected by Kanel *et al.*[2] This recompression can be interpreted as a wave reflection from the failure wave front due to a mechanical impedance reduction in the material behind the failure wave. The second type of experiment, spall experiments, provided further insight into this phenomenon. The experiments showed that if the spall plane is located in front of the failure wave, the material exhibits a finite spall strength. By contrast, if the spall plane is located behind the failure boundary, the spall strength is significantly reduced. An important finding reported in the work by Brar and Bless[4] is that an impact stress above a threshold of approximately 4 GPa is required to produce failure waves in soda–lime glass. Furthermore, transverse stress measurements performed with lateral in-material gauges showed an increase in transverse stress upon the arrival of the failure wave to the gauge location. These results clearly indicate the so-called failure wave is actually a moving boundary of damaged material within the specimen. As a matter of fact, the increase in lateral stress and the partial or complete loss of spall strength behind this boundary clearly indicate the material has undergone extensive inelasticity.

Several mechanisms have been invoked to explain the initiation and propagation of failure waves. Based on the fact that room-temperature plasticity in amorphous materials is highly inhomogeneous (see, for instance, Speapen,[5] Argon,[6] and Steif *et al.*[7]) Espinosa and Brar[8] postulated that in the case of plate

J. J. Petrovic—contributing editor

Manuscript No. 192352. Received September 1, 1995; approved August 28, 1996.
This research was supported by the National Science Foundation through Grant Nos. MSS-9309006 and MSS-9311289 and by the Purdue Research Foundation through grant No. 690-1282-2001. The experimental work at UDRI was sponsored by the U.S. Army Research Office under Contract No. DAAL03-88-K-0203.
*Member, American Ceramic Society.

experiments, the inelastic mechanism leading to the so-called failure waves is inhomogeneous plastic flow. They suggested that atomic defects present on glass plate surfaces are likely sites for the development of stress concentrations necessary for formation of shear-induced flow surfaces. Within this interpretation, the reported reduction in dynamic tensile (spall) strength behind the failure wave is the result of the extension of microcracks nucleated at the intersection of the shear flow surfaces. This appears to be a plausible mechanism in view of the fact that bulk soda–lime glass does not undergo shear-induced plastic deformation for shear stresses up to 3.2 GPa.[9] Furthermore, observations of crack nucleation in indentation studies on soda–lime glass[10,11] support this mechanism for crack initiation under fully compressive stress states (all three principal stresses are negative).

Two hypotheses for explaining failure waves were examined by Raiser and Clifton.[12] The first invokes the initiation of cracks at the impact surface, due to local stresses around asperities, which can propagate approximately at 45° to the impact face (see also Kanel *et al.*[13]). The second assumes phase transformations to crystalline phases within the bulk of the glass samples. Since their experimental results show that surface roughness appears to play no role in the formation of failure waves and that glass spallation at the failure boundary and its vicinity is progressive, they concluded that the failure wave phenomenon may be the result of phase transformations within the glass. Because of difficulties in recovering the shocked samples, no direct evidence was given to support these hypotheses.

The challenges of finding a micromechanical explanation and modeling failure waves in amorphous materials still remain. It is the objective of the present work to provide additional experimental evidence that can allow the identification of the failure mechanism. The paper starts with a comprehensive review of plate (1-D strain) and rod (1-D stress) impact experiments performed on several glasses. New experimental records obtained in normal, pressure-shear, and confined rod recovery experiments will be presented and discussed. Numerical simulations of these experiments, with a microcracking multiple-plane model, will be presented in a second paper. The simulations will show that a population of planar defects, growing under the dynamic stress state, can capture the essential features recorded in plate and rod experiments. Furthermore, it will be shown that microcracking appears to be the mechanism responsible for the observed reduction in spall strength, behind failure waves. Differences in crack initiation sites in plate and rod experiments will be presented and explained. These results will provide the framework needed for a consistent explanation of the observed failure wave phenomenon in glass rods and plates.

II. Experimental Method

(1) Materials

Soda–lime glass plates (5.7 mm thick) were obtained locally. The density and longitudinal wave velocity were 2.5 g/cm^3 and 5.84 mm/μs, respectively. Corning 1723 aluminosilicate glass plates and Pyrex bars 12.7 mm in diameter were obtained from Corning Inc., Corning, NY. The aluminosilicate glass properties were as follows: density = 2.64 g/cm^3, Young's modulus = 86 GPa, and Poisson's ratio = 0.24. The Pyrex density was 2.23 g/cm^3 and its longitudinal wave velocity was 5.6 mm/μs. The in-material measurements were performed with commercial manganin gauges purchased from Micro-Measurements, Raleigh, NC.

(2) Spall Strength and Longitudinal Gauge Experiments

The target configuration used in spall experiments is shown in Fig. 1(a). A manganin gauge was embedded between the

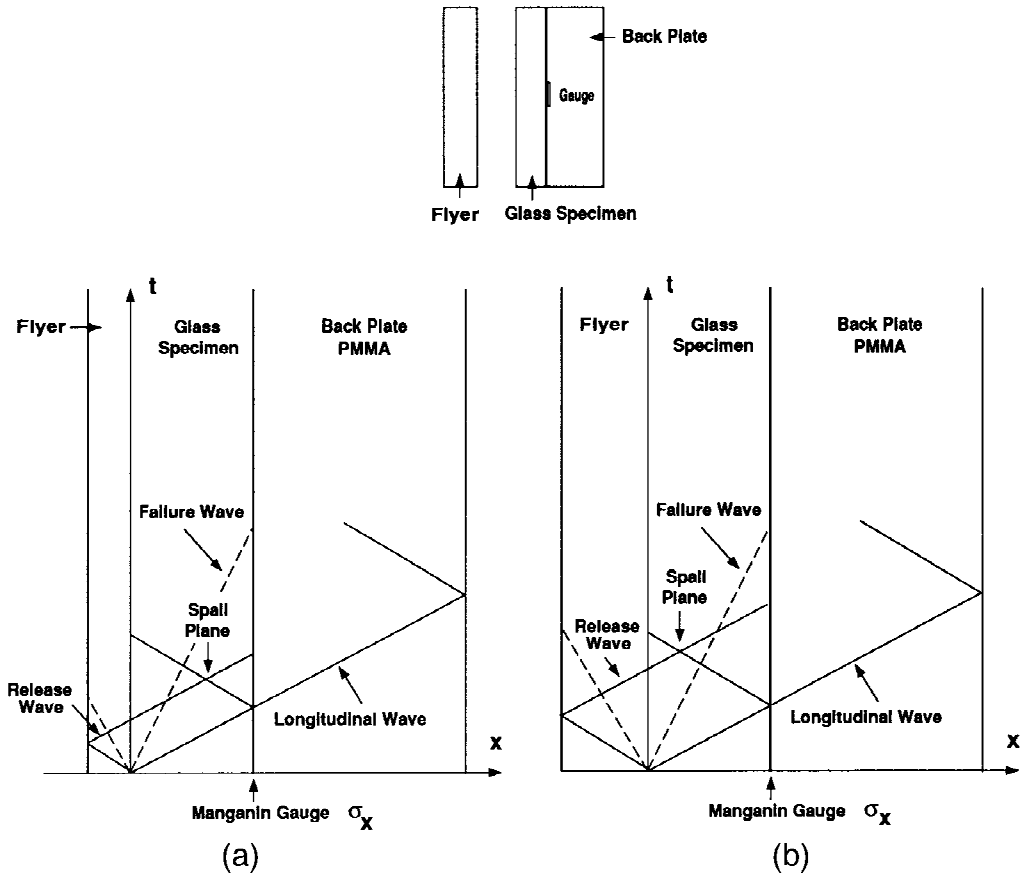

Fig. 1. Distance–time plot for plate normal impact experiments: (a) spall plane in front of failure wave; (b) spall plane behind failure wave.

glass specimen and a 12 mm thick PMMA back plate to record longitudinal stress histories, σ_1–t. Aluminum and copper flyers with different thicknesses were chosen to produce spall planes behind and in front of the failure boundary. The effect of flyer thickness on the spall plane location can be seen in the Lagrangian time–position (t–X) diagrams shown in Fig. 1(b). One can observe that by changing the flyer plate thickness, the position at which the two unloading waves, one from the flyer back surface and the other from the specimen–PMMA interface, meet can be selected to be behind or in front of the failure wave front. Impactor velocities were set to obtain peak shock stresses below and above HEL.

In-material axial stress measurements were performed by embedding a manganin gauge between two glass plates at a distance between 1.5 and 3 mm from the impact plane. To minimize gauge failure, upon arrival of the failure wave to the gauge location, a gauge package consisting of three mylar sheets, 0.001 in. thick, and a manganin gauge was utilized. The gauge package was glued and statically pressed between two glass plates to minimize its thickness and hence improve its time resolution.

(3) Transverse Gauge Experiments

In these experiments one or two narrow, 2 mm wide, manganin gauges (Type C-8801113-B) were embedded in the glass target plates in the direction transverse to the shock direction as shown in Fig. 2. A thick back plate of the same glass was used in the target assembly. Aluminum or glass impactor plates were used to induce failure waves. The transverse stress, σ_2, was obtained from the transverse gauge record. A major concern with this technique is the perturbation of the one dimensionality of the wave propagation due to the presence of a thin layer, perpendicular to the wave front, filled with a material having a different impedance and mechanical response. Calculations by Wong and Gupta[14] show that the inelastic response of the material being studied affects the gauge calibration. Recently, Rosenberg and Brar[15] reported that in the elastic range of the gauge material, its resistance change is a function of the specimen elastic moduli. In a general sense, this is a main disadvantage in the lateral stress gauge concept. By contrast, their analysis shows that in the plastic range of the lateral gauge response, a single calibration curve for all specimen materials exists. These findings provide a methodology for the appropriate interpretation of lateral gauge signals, and increase the reliability of the lateral stress measuring technique.

(4) Pressure-Shear Experiments

Dynamic compression-shear loading can be obtained by inclining the flyer and target plates with respect to the axis of the projectile. By varying the angle of inclination a wide variety of nonproportional loading can be obtained. A particularly useful pressure-shear configuration is shown in Fig. 3. In this configuration high shear strain rates and pressures are achieved by impacting a thin specimen sandwich between a hard flyer and a hard anvil plate. WC/6Co flyer and anvil plates were used in this study, such that the plates remained elastic up to the imposed stress levels. Stresses, shear strains, and strain rates can be obtained by measuring the longitudinal and transverse particle velocities at the anvil back surface. A normal velocity interferometer (NVI) and a transverse displacement interferometer (TDI) were used for this purpose. Measured transverse particle velocities are used to identify the glass dynamic shear resistance at strain rates of the order 10^5/s and pressures between 5.9 and 8.2 GPa. Further details about this experimental configuration applied to the study of brittle materials can be found in Espinosa and Clifton.[16]

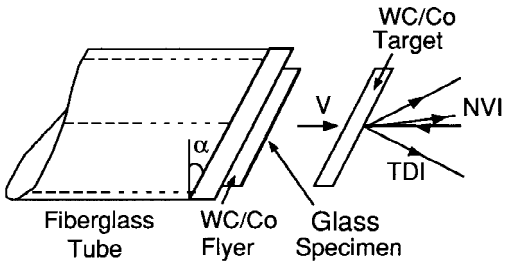

Fig. 3. Pressure-shear high-strain rate configuration.

(5) Unconfined Bar Impact Experiments

The objective of these experiments was to extend uniaxial strain deformation states imposed in plate impact experiments. The possibility of generating a variety of multi-axial deformation states appears to be very relevant to the characterization of failure mechanisms in brittle materials. It not only provides a direct measurement for the yield stress at rates of 10^3 to 10^4/s, but also allows the examination of constitutive models and numerical solution schemes under 2-D fields. In-material stress measurements, with embedded manganin gauges, are very useful in providing axial stress histories that otherwise cannot be obtained. Stress decay, pulse duration, release structure, and wave dispersion are very well defined by these measurements. Bars, 127 mm long, were impacted with thick steel plates or glass bars as shown schematically in Fig. 4. The bar surfaces were finely ground to a smooth finish and there were no visible surface flaws. One-dimensional stress was measured by embedding manganin gauges (Type C-880113-B) approximately 10 diameters away from the impact face. Gauge profiles were interpreted using the calibration given in Rosenberg and Partom.[17] The gauges were baked by 50.8 mm long pieces of bars of the same material as the front piece. The back pieces of the assembled bar targets were set in a lexan disk using epoxy in order to align the target for a planar impact. A coaxial trigger pin was also set through a hole in the lexan ring to trigger a manganin gauge bridge circuit and a high-speed camera. An

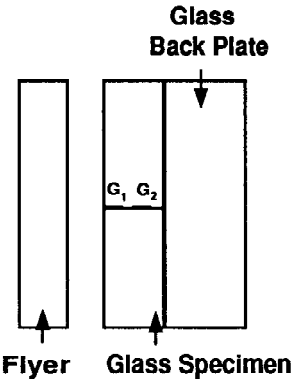

Fig. 2. Transverse gauge experimental configuration.

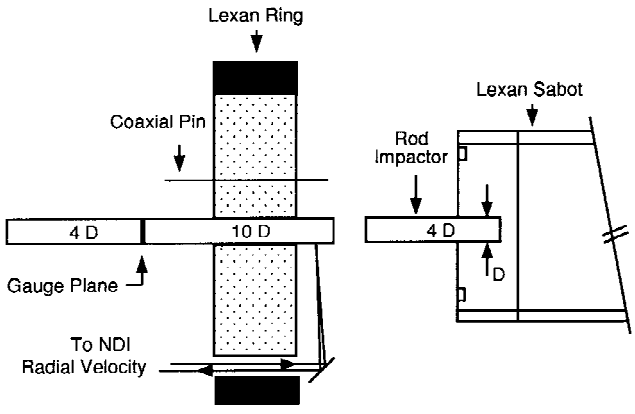

Fig. 4. Unconfined bar experimental configuration.

Imacon 790 high-speed framing camera was used to monitor the propagation of failure fronts.

(6) Bar Impact Recovery Experiments

The confined bar on bar impact experiment, shown in Fig. 5, is a very useful technique for studying failure mechanisms in brittle materials. A symmetric impact allows the recovery of the impactor bar and hence the possibility of performing microscopy studies that can provide insight into the failure mechanisms responsible for features observed in interferometrically measured velocity histories. Free surface velocity measurements at the rod end basically provide the strength of the transmitted compressive wave and the pullback signal due to bar spalling. Since stress attenuation occurs when the material is damaged, a reduction in microcracking as a function of position is observed in most brittle materials.[18] Therefore, we have performed radial velocity measurements close to the impact surface to provide the best information on damage rate and accumulation throughout the history of deformation. If damage occurs everywhere in the rod, radial velocity measurements at several diameters of the impact surface can also be very useful in damage identification.

Details of the experimental configuration are shown in Fig. 5. Soda–lime bars were embedded in 4340 steel sleeves, 1 in. in diameter, to provide lateral confinement and minimize fracture due to radial wave release. The inside diameter of the steel sleeve was machined with a tolerance of +25.4 μm. During the assembly of the glass rod and steel sleeve, a thin layer of epoxy mixed with fine alumina powder was used at the glass–steel interface. The target bar was positioned by a foam ring which was mounted to a target holder with alignment capabilities. The projectile consisted of another identical bar of the same materials approximately 5 diameters in length. This bar was mounted to a nylon holder which was launched by means of a 3-in. fiber glass projectile. The target bar was aligned for planar impact,[19] and tilt pins were used to measure tilt and to trigger a recording oscilloscope. Radial and normal velocities were recorded by means of displacement and velocity interferometers, respectively. The impactor was stopped by a steel anvil which was designed to trap the kinetic energy of the projectile.

III. Experimental Results

The impact parameters used in all of the above experiments are summarized in Table I. In Table II we report a series of transverse gauge experiments performed on soda–lime glass. In all of these experiments 6061-Aluminum flyer plates, 11.3 mm thick and 2 in. in diameter, were launched against 12.6 mm thick soda–lime glass targets backed by 5.7 mm thick soda–lime glass plates. Measured profiles of manganin gauges were converted to stress–time profiles following the calibrations of longitudinal and transverse manganin gauges under shock loading given in Rosenberg and Partom[17] and Rosenberg and Brar,[15] respectively.

(1) Glass Plates

Evidence of the existence of failure waves in glass comes from spall and transverse gauge experiments. We mentioned earlier that the spall strength of glass is a function of the location of the spall plane within the sample. In experiment 7-0889 we impacted a 5.7 mm thick soda–lime glass target with a 3.9 mm aluminum flyer at a velocity of 906 m/s. The manganin gauge profile is shown in Fig. 6. The spall plane in this experiment happened to be behind the failure wave. The profile shows the arrival of the compressive wave with a duration of approximately 1.5 μs, followed by a release to a stress of about 3 GPa and a subsequent increase to a constant stress level of 3.4 GPa. The stress increase after release is the result of reflection of the tensile wave from material that is being damaged under dynamic tension and represents the dynamic tensile strength of the material (spall strength). From this trace we conclude that soda–lime glass shocked to a stress of 7.5 GPa has a spall strength of about 0.4 GPa behind the so-called failure wave. We repeated this experiment with a 2.4 mm thick aluminum flyer (7-1533) and found complete release from the back of the aluminum impactor (see Fig. 6). A pullback signal is observed after approximately 0.45 μs with a rise in stress of about 2.6 GPa. It should be noted that the spall plane in this experiment was in front of the failure wave. These two experiments clearly show that the spall strength of glass depends on the location of the spall plane with respect to the propagating failure wave. For soda–lime glass dynamic tensile strengths of 2.6 and 0.4 GPa are measured in front and behind the failure wave, respectively.

In order to observe whether a failure wave in soda–lime glass occurs for peak stresses in the elastic range (below HEL), we analyzed the data from four experiments (7-0892, 7-1612, 7-1615, 7-1623; see Table I). Impactor thicknesses in experiments 7-1612, 7-1615, and 7-1623 were chosen so that the spall plane was behind the failure wave. Manganin gauge profiles from these experiments show unambiguously that the spall strength of soda–lime glass was significantly reduced behind the failure wave. In experiment 7-0892, in which the spall plane was in front of the failure wave, a spall strength of 3.0 GPa was measured. Thus, the results on the spall strength of soda–lime glass for the same shock stress in the elastic range are drastically different. These differences can be resolved on the basis of the existence of failure waves in soda–lime glass for shock stresses below and above HEL.

Additional features of the failure wave phenomenon were obtained from transverse gauge experiments performed recently on soda–lime and aluminosilicate glasses. Figure 7 shows measured transverse gauge profile at two locations (shot-7-1719) in the Corning 1723 glass. One can clearly see

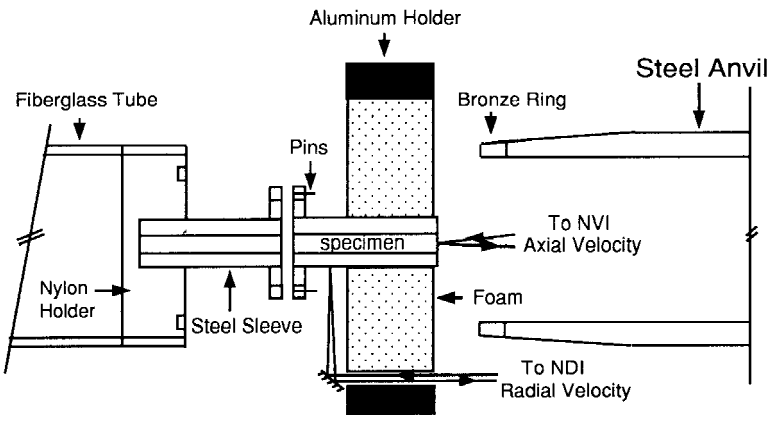

Fig. 5. Bar recovery experimental configuration.

Table I. Summary of Experimental Data†

Shot no.	Exp. Conf.	Impactor/Thickness (mm)	Target/Thickness (mm)	Impact velocity (m/s)	Normal stress (GPa)	Remarks
7-0889	SS	Al/3.9	SLG/5.7	906	7.5	Reduced spall strength
7-1533	SS	Al/2.4	SLG/5.7	917	7.6	No spall signal; full unloading
7-1717	LG	Al/12.7	CG/19.4	770	6.1	Transverse stress increase
7-1719	LG	A1/14.5	CG/19.4	878	6.97	Transverse stress increase
7-1754	NI	Al/2.4 + WC/9.0	SLG/3+gauge+ SLG/12	513	3.99	Progressive stress decay upon arrival of failure wave
7-0892	NI	A1/3.1	SLG/5.7	745	5.7	No spall signal; full unloading
7-1612	NI	Al/5.2	SLG/5.7	728	5.5	Reduced spall strength
7-1615	NI	Al/4.8	SLG/5.7	741	5.7	Reduced spall strength
7-1623	NI	SLG/4.8	SLG/5.7	681	4.9	Reduced spall strength
7-1732	NI	4340S/12.7	CG/1.57+gauge+ CG/8.76	746	7.2	Progressive stress decay upon arrival of failure wave
7-1763	NI	Al/12.7	CG/3.17+gauge+ CG/12.0	740	6.1	Glass densification
91-08	HRPC, $\alpha = 18^0$	AlN/4.08+WC/3+ CG/0.24	WC/5.62	212	11.0	Shear resistance $\tau = 880$ MPa at a pressure of 9.6 GPa
91-10	HRPS, $\alpha = 18^0$	WC/9.38+CG/0.324	WC/5.93	116	6.0	Shear resistance $\tau = 700$ MPa at a pressure of 6.0 GPa
91-11	HRPS, $\alpha = 15^0$	WC/9.3+CG/0.22	WC/5.79	162	8.5	Shear resistance $\tau = 850$ MPa at a pressure of 8.5 GPa
7-1661	UR	SLG/76.2, 13.97 dia.	Al/1.6+SLG/127, gauge+SLG/50.8	210	1.0	Axial stress attenuation due to failure wave
4-1127	CRR	SLG-4340S/50.12	SLG-4340S/49.9	171	2.0	Glass fragmentation
4-1008	CRR	4340S/50.2	SLG-4340S/ 49.8+4340S/40	495	5.5	Glass fragmentation
7-1312	UR	Steel Plate/15, 50.4 dia.	Pyrex/150+gauge+ Pyrex/46.4	210	1.5	Observation of failure wave with high-speed photography
7-1386	UR	Pyrex/63.5, 12.7 dia.	Pyrex/127	336		Observation of failure wave with high-speed photography
7-1387	UR	Pyrex/63.5, 12.7 dia.	Pyrex/127+gauge+ Pyrex/25	227	1.4	Observation of failure wave with high-speed photography
7-1388	UR	Pyrex/63.5, 12.7 dia.	Pyrex/127+gauge+ Pyrex/25	125	0.9	Observation of failure wave with high-speed photography

†SS = spall strength; LG = lateral gauge; UR = unconfined rod; HRPS = high-strain-rate pressure-shear; CRR = confined rod recovery; HRPC = high-strain-rate pressure change; α = skew angle; NI = normal impact; Al = aluminum; SLG = soda–lime glass; CG = corning glass; AlN = aluminum nitride; 4340S = 4340 steel; WC = tungsten carbide/6 Co.

Table II. Summary of Experimental Data on Shear Strength

Shot no.	Imp. vel (m/s)	σ_1 (GPa)	σ_2 (GPa)		τ (GPa)	
			Front	Behind	Front	Behind
7-1651	514	3.8	1.07	—	1.37	—
7-1658	569	4.7	1.6	2.4	1.55	1.15
7-1653	727	5.5	2.0	3.3	1.75	1.1
7-1644	822	6.3	2.3	4.3	2.0	1.0
7-1645	823	6.3	2.2	4.0	2.0	1.15

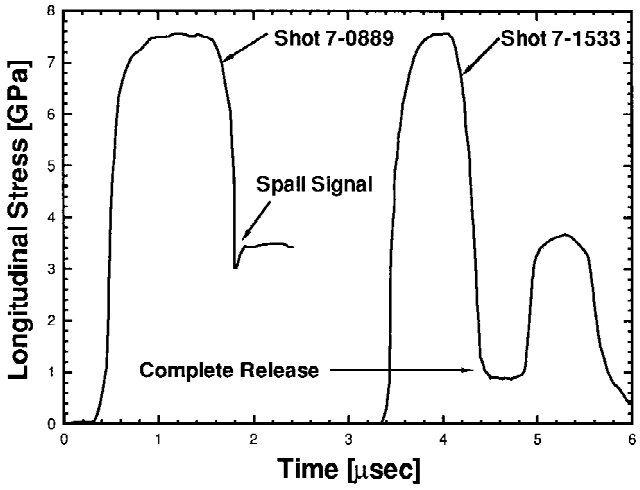

Fig. 6. Gauge profile from experiment 7-0889 showing reduced spall strength. Gauge profile from experiment 7-1533 showing complete release and a spall strength of 2.6 GPa.

the two-wave structure which results from the failure wave following the longitudinal elastic wave. The first gauge, at the impact surface, shows an increase in lateral stress to the value predicted by 1-D wave theory, 2.2 GPa in Fig. 7, immediately followed by a continuous increase to a stress level of 4.2 GPa. The second gauge, at 3 mm from the impact surface, initially measures a constant lateral stress of 2.2 GPa followed by an increase in stress level on arrival and passage of the failure wave. It should be noted that gauge G1 records a continuous increase in lateral stress up to 4.2 GPa. This can only be the case if the failure wave has an *incubation time* of less than 250 ns (rise time of the lateral stress to the elastic prediction of 2.2 GPa). By contrast, gauge G2 sees the arrival of the failure wave about 700 ns after the arrival of the elastic wave (see step at 2.2 GPa). Furthermore, these traces also confirm that the failure wave initiates at the impact surface and propagates to the interior of the sample. This interpretation is in agreement with the impossibility of monitoring impact surface velocity with a VISAR system, see Dandekar and Beaulieu,[20] when failure waves are present.

An estimate of the failure wave speed can be obtained from the first lateral gauge history; for instance, see the front gauge history for experiment 7-1719 (Fig. 7). In fact, the width of the gauge is 2 mm and the duration of the stress increase, from 2.2 GPa to the plateau level of 4.2 GPa, is about 1 ± 0.1 μs. This time is taken by the failure wave to sweep across the 2 mm width of the gauge. Thus, the failure wave speed is about 2 ± 0.2 mm/μs, which is similar to the failure wave speed measured in soda–lime glass by Brar and Bless[4] following this procedure. On the other hand, if the larger slope in the initial portion of the transverse stress history at the first gauge (see

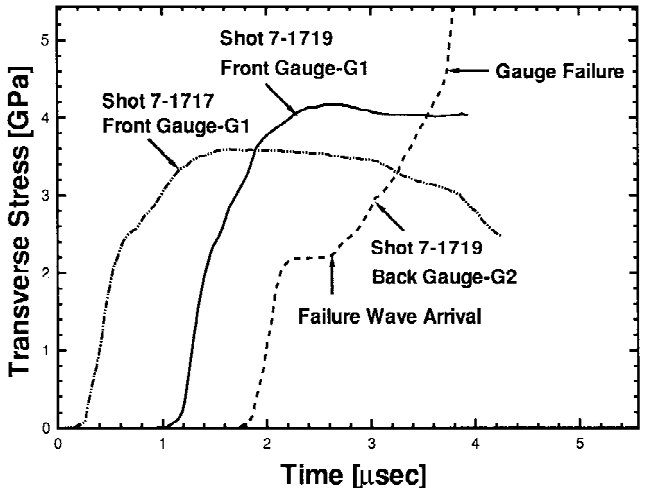

Fig. 7. Manganin gauge records from shots 7-1717 and 7-1719, showing transverse stress histories at two locations (see Fig. 2 for location of transverse gauges).

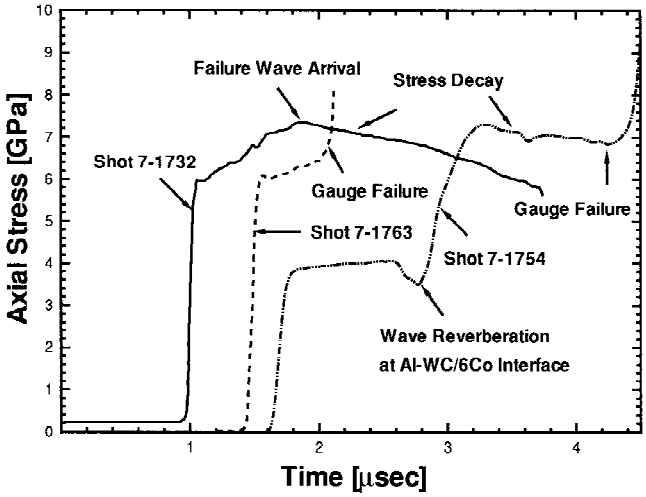

Fig. 8. Longitudinal stress histories from shots 7-1732, 7-1754, and 7-1763. Threshold stress for glass densification and progressive axial stress decay behind failure wave are observed.

front and back gauge signals) is interpreted as the instantaneous formation of the failure wave, the sweeping time through the gauge is about 1.3 μs. Hence, the failure wave speed becomes 1.54 mm/μs instead of 2 mm/μs. This latest value is similar to the failure wave velocity measurements performed by Dandekar and Beaulieu[20] in soda–lime glass. Furthermore, their experimental results indicate the failure wave velocity remains constant with the thickness of the glass at an impact stress of 5.2 GPa.

The increase in transverse stress, behind the failure wave front, can be interpreted as a significant drop in shear strength. In Table II we report the shear strength of soda–lime glass, $\tau = (\sigma_1 - \sigma_2)/2$, both in front of and behind the failure wave. The data for the shear strength of glass in front of the failure wave fall on the elastic line drawn to the HEL. However, the shear strength behind the failure wave is about 1.1 GPa for shock stresses above 4 GPa. We interpret this dramatic reduction in shear strength of glass to be the result of inelasticity behind the failure wave in the form of inhomogeneous flow. Furthermore, the increase in lateral stress behind the failure wave raises the mean stress, $\frac{1}{3}(\sigma_1 + 2\sigma_2)$, indicating the existence of a significant inelastic strain in the lateral direction. As will be shown in a second paper, these inelastic strains appear to be the result of the growth of defects (e.g., shear-induced flow surfaces) under a fully compressive stress state.

In order to investigate the axial stress history behind the failure wave, several in-material gauge experiments were conducted with manganin gauges embedded between two glass plates at 1.5 and 3 mm from the impact plane. By locating the gauge close to the impact surface, information concerning the longitudinal stress history behind the failure wave can be obtained. In most experiments, gauge failure occurred upon arrival of the failure wave to the gauge location, especially, if mylar sheets were not used in the gauge package.

In Fig. 8 axial stress histories recorded in experiments 7-1732, 7-1763, and 7-1754 are plotted. In experiment 7-1732, a manganin gauge was embedded between two Corning 1723 glass plates at 1.57 mm from the impact plane. The axial stress recorded in this experiment shows a stress jump to a level of 6 GPa followed by a progressive axial stress increase up to a peak stress of approximately 7.2 GPa. This feature is associated with glass densification and wave reverberations within the gauge package (approximately 150 μm thick). A similar stress jump is observed in experiment 7-1763. Hence, based on our interpretation of the HEL as the onset of permanent densification, we can state that the Hugoniot elastic limit of the Corning 1723 aluminosilicate glass is 6 GPa. In experiment 7-1732, a progressive reduction in axial stress is observed after 0.87 μs of the initial stress jump. This stress reduction can be attributed to the arrival of the failure wave to the gauge location. A failure wave speed of about 1.8 mm/μs is inferred from this record.

A double shock experiment, shot 7-1754, was performed to further investigate the strength of the material behind the failure wave front, and to confirm the existence of a stress threshold for failure wave development. A double plate flyer made of aluminum and WC/6Co impacted a soda–lime glass target containing a manganin gauge embedded at 3 mm from the impact surface. The in-material measurement of longitudinal stress is plotted in Fig. 8. Upon arrival of the first compressive wave at the gauge location, the axial stress rises to a plateau value of about 4 GPa. In this case, no evidence of a compaction wave propagating in the soda–lime glass is observed. The longitudinal stress remains approximately constant until a small unloading followed by a stress increase is observed. This small unloading results from the low impedance of the glue used to bond the two flyer plates. The second compressive pulse, arising from the higher impedance of the WC/6Co plate, has a peak stress of approximately 7.3 GPa. Further examination of the second pulse shows a progressive reduction in longitudinal stress, likely due to arrival of the failure wave to the gauge location. This feature is similar to the one observed in experiment 7-1732 and indicates that a failure wave was initiated by the first compressive pulse. In fact, the first compressive pulse has a magnitude of approximately 4 GPa, which is about the threshold stress for failure wave formation in soda–lime glass.

The progressive reductions in axial stress upon arrival of the failure wave at the gauge location, which are observed in experiments 7-1732 and 7-1754, suggest that the inelastic process responsible for the reduction in material shear strength has well-defined kinetics. These experimental records are especially suitable for the examination of constitutive models describing damage evolution behind the failure wave. In a second paper we will examine these features by performing numerical simulations with a multiple-plane microcracking model. Another implication of this result is the fact that the shear strength behind the failure wave is actually smaller than the one reported in Table II because in those calculations the peak elastic longitudinal stress, σ_1, was used. A more accurate value requires the knowledge of both σ_1 and σ_2 histories at the same spatial point. Such histories are difficult to obtain with the in-material gauge technique.

More direct experimental information concerning the shear resistance of glass was obtained by means of pressure-shear high-strain-rate experiments. The results corresponding to

three experiments are summarized in Table I. Values of pressure, shear stress, and shear strain rate are reported at times prior to the arrival of unloading waves from the plate periphery. The normal and transverse velocities recorded for shot 91-08 are given in Figs. 9(a) and (b), respectively. This experiment makes use of the high-strain-rate, pressure-change configuration described in Espinosa and Clifton.[16] The existence of a gap at the glass-flyer interface is evident from the partial unloading of the normal wave after 95 ns. Upon closure of the gap, the normal velocity monotonically increases up to the attainment of a state of homogeneous deformation. A reduction in pressure is observed to start at 950 ns until a spall signal begins to increase the normal velocity. The origin of such a signal is understood to be the result of tensile failure of the WC/6Co anvil plate resulting from the pure shear stress state that develops after unloading of the longitudinal wave (Espinosa and Clifton[16]). This mode of failure prevents the transmission of the shear wave emanating from the glass–WC/6Co interface, and leads to a premature reduction of the transverse particle velocity (see Fig. 9(b)). Nonetheless, the shear stress history is long enough to develop a short plateau at a stress level of about 840 MPa, which is well below the shear stress that should be achieved in the absence of inelastic deformation. The experimental records obtained from shot 91-11, plotted in Figs. 9(a) and (b), provide further information on the high-strain-rate deformation of Corning glass. The normal velocity presents features similar to the normal velocity recorded in shot 91-08, except that in this case no change in pressure is observed after the homogeneous state of deformation has been reached. A maximum normal stress of 8 GPa is achieved well above the reported threshold stress for the formation of failure waves. Hence, since the sample thickness is only 300 μm, we expect the failure wave to propagate through the entire sample by the time the homogeneous deformation state develops. The shear wave profile shows an increase in stress to a level of about 200 MPa with a small stress reduction after 200 ns, resulting from the reduction in normal stress at the specimen–anvil interface. Subsequently, the shear stress rises to a plateau value of 880 MPa. This stress level is well below the stress level predicted by one-dimensional elastic wave theory which clearly shows the achievement of a state of inelastic deformation in the glass specimen.

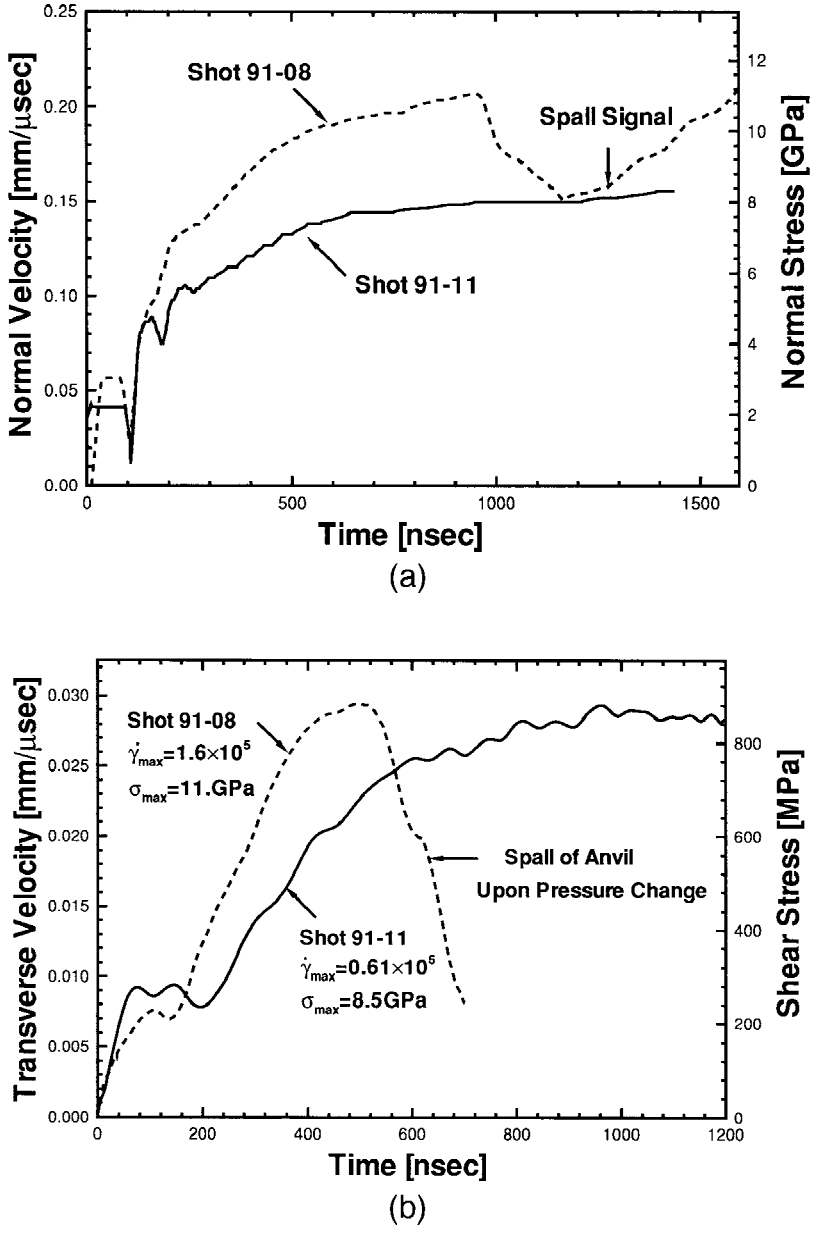

Fig. 9. (a) Normal velocity at the free surface of the anvil and normal stress at the specimen–anvil interface. Experiments 91-08 and 91-11. (b) Transverse velocity at the free surface of the anvil and shear stress at the specimen–anvil interface. Experiments 91-08 and 91-11.

By comparing the maximum shear stresses attained in the two pressure-shear experiments previously described, a weak strain-rate sensitivity of the flow stress is inferred. An important implication of these measurements is the fact that the measured shear stress during the state of homogeneous deformation, $\tau = 0.88$ GPa, is in close agreement with the shear stress behind the failure wave measured in normal impact experiments. This feature implies the shear stress interferometrically recorded in the pressure-shear experiments corresponds to the dynamic behavior of damaged glass. We will further examine this point by performing numerical simulations of these experiments with a microcracking multiple-plane model. Another feature revealed by the pressure-shear experiments is that the shear resistance of glass is pressure dependent. It has been observed that the shear resistance of aluminosilicate glass increases from 700 to 800 MPa when the pressure increases from 6 to 9.6 GPa (see Table I).

(2) Glass Bars

A sequence of photographs taken in an unconfined soda–lime glass bar experiment, shot 7-1661, are shown in Fig. 10. The photographs were taken at 10 μs/frame. A fiducial wire is located 25 mm from the impact face. Impact occurs between the third and fourth frames, and the fracture front originating at the impact face propagates about 50 mm away from the impact face in the fifth frame. A failure wave speed of approximately 3.6 mm/μs is estimated from these photographs. In frame 7 initiation of a second fracture front from the interface at the gauge location is seen. This second fracture front propagates about 40 mm toward the impact face, as seen in the eighth frame and stops. The first fracture front propagates about 75 mm along the bar and stops as well. A 20 mm long segment of the target bar remains intact throughout the observation time of 160 μs. The manganin gauge profile from this shot is shown in Fig. 11. Unloading of the stress wave takes place from the far end of the 50.8 mm bar at approximately 22 μs. This profile shows a peak stress of 1 GPa, whereas the calculated stress, assuming elastic material response, is 1.4 GPa.

High-speed photography was also used in rod-on-rod experiments to investigate the stress dependence of the failure wave speed. The position of the failure wave as a function of impact velocity, for Pyrex rods, is shown in Fig. 12. Failure wave velocities were 2.3 and 5.2 mm/μs in Pyrex bars when impacted with a Pyrex bar at 125 and 336 m/s, respectively, and 4.5 mm/μs when impacted with a steel plate at 210 m/s. Impact stresses corresponding to impact velocities of 125, 227, and 336 m/s for the glass bar on bar tests, from impedance matching, are about 0.8, 1.4, and 2.0 GPa, respectively. In the test where a steel plate impacts a glass bar at 210 m/s, the impact stress is 1.9 GPa. The higher failure wave velocity of 4.5 mm/μs at similar impact velocity is perhaps due to the higher impact stress in the case of steel–Pyrex impact. This result suggests that failure wave velocity in unconfined bars is a simple function of impact stress.

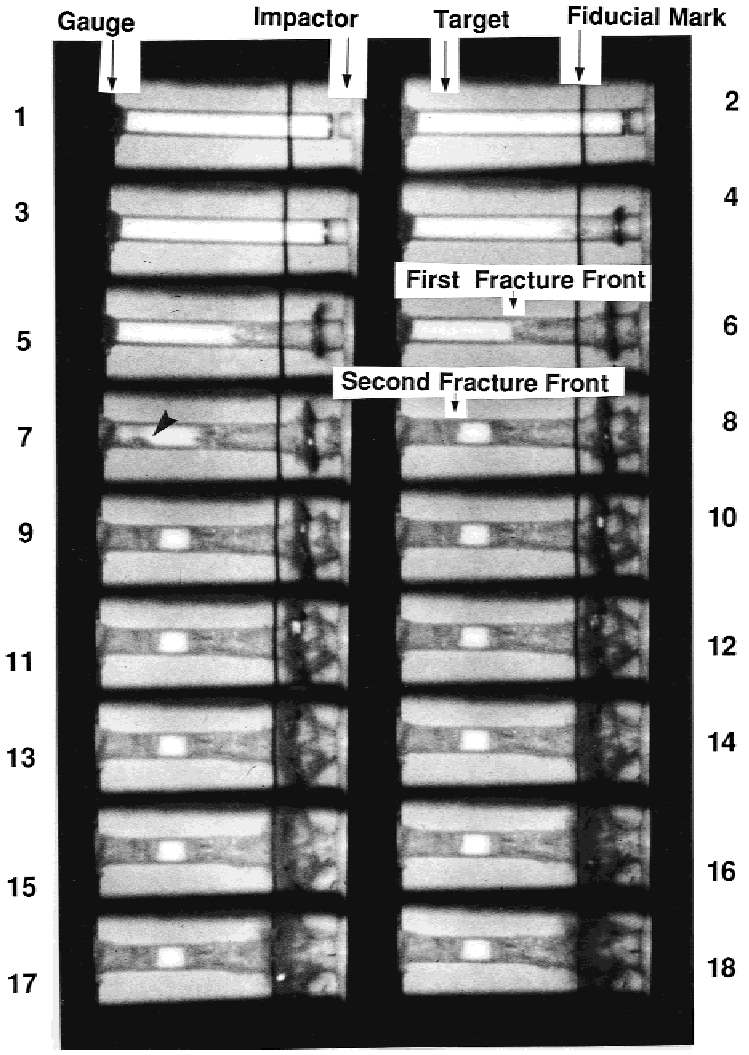

Fig. 10. Framing camera pictures of a fracture front in a 13.97 mm diameter soda–lime glass bar on impact with a bar at 210 m/s.

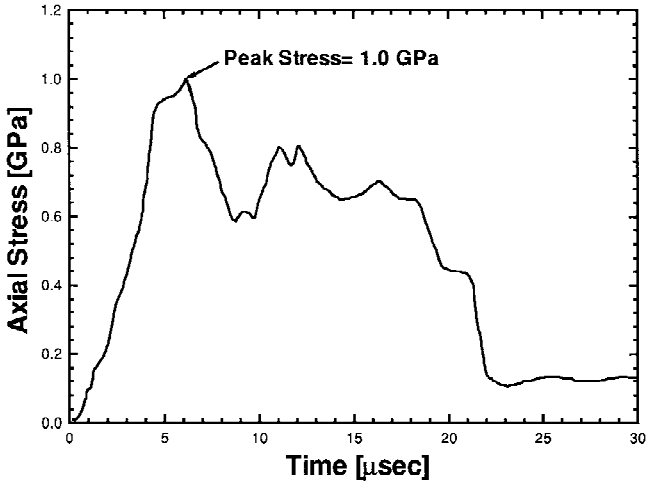

Fig. 11. Manganin gauge profile from experiment 7-1661.

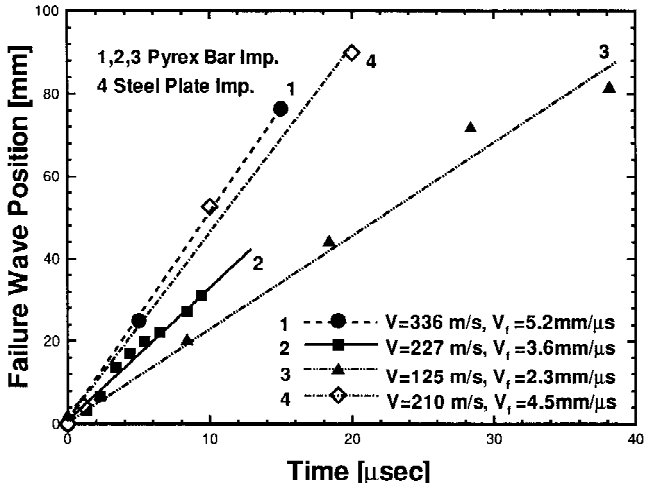

Fig. 12. Failure wave position in 12.7 mm diameter Pyrex bars as a function of impact velocity.

We next discuss the results of a bar recovery experiment performed on soda–lime glass bars. In this experiment 4340 steel sleeves confined the shock loaded soda–lime glass bars. The radial velocity history recorded in shot 4-1127, at 15 mm from the impact surface, is plotted in Fig. 13. This radial velocity was obtained by means of a normal displacement interferometer using a laser beam focused on the steel sleeve surface. The trace starts with a radial velocity of approximately 14 m/s followed by a rising part with a peak velocity of 28 m/s. A progressive reduction in radial velocity with well-defined cusps is observed. At approximately 18 μs, the velocity becomes negative, reaching a minimum of 14 m/s. This feature can be correlated with the arrival of an unloading wave from the bar end. Numerical simulations to be discussed in a second paper will show that the slope of the cusped curve, following the initial peak, is controlled by the rate of damage in the soda–lime rod.

An optical micrograph of the recovered rods is shown in Fig. 14. The rod on the left shows the impact surface of the target bar, while the rod on the right is a view of the back surface of the impactor rod. In both views, a highly fractured core surrounded by an outer ring containing split cracks is observed. The presence of split cracks on the outer ring indicates that cracks are nucleated at the bar periphery. It should be noted that an approximately 0.001 in. gap, filled with a mixture of alumina powder and epoxy, existed between the soda–lime rod and the steel sleeve. The presence of this gap may have contributed to the formation of the outer ring. The finely fragmented core seems to be more representative of microcracking under 1-D deformation (fully compressive stress state).

Post-test examination of the glass rod revealed that the entire glass rod underwent significant microcracking. In Fig. 15, a micrograph showing the crack pattern on the recovered rod surface is shown. Cracks almost perpendicular and parallel to the bar axis form fragments of various sizes. A micrograph taken on the rod back surface shows typical features observed in glass fracture. Several twist hackles due to lateral twist in the tension axis are observed (see Fig. 16). Wallner lines (see Frechette[21]) generated by interaction of elastic pulses emanating from other crack fronts and the advancing crack tip on the plane of the picture are also observed on the left of the micrograph.

When observations are made within the bar core 10 mm from the impact surface, several features emerge. Radial patterns

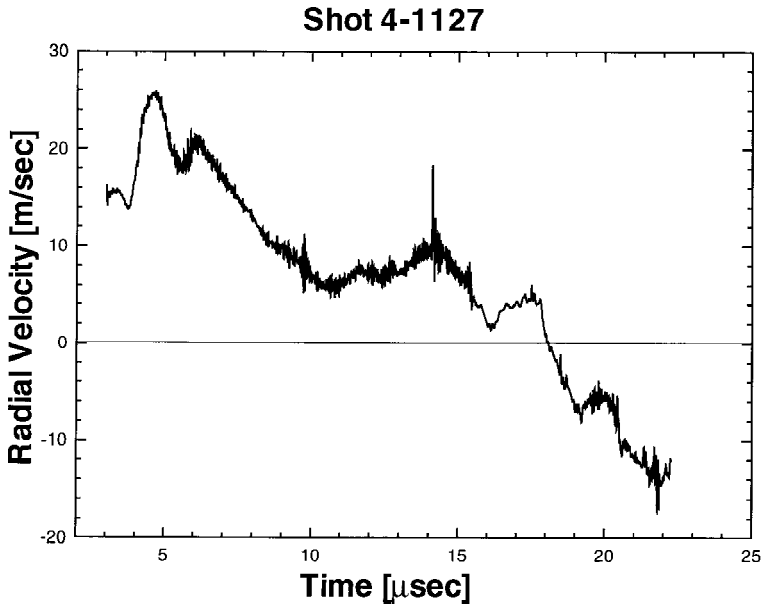

Fig. 13. Radial velocity history at 15 mm from the impact surface recorded in experiment 4-1127.

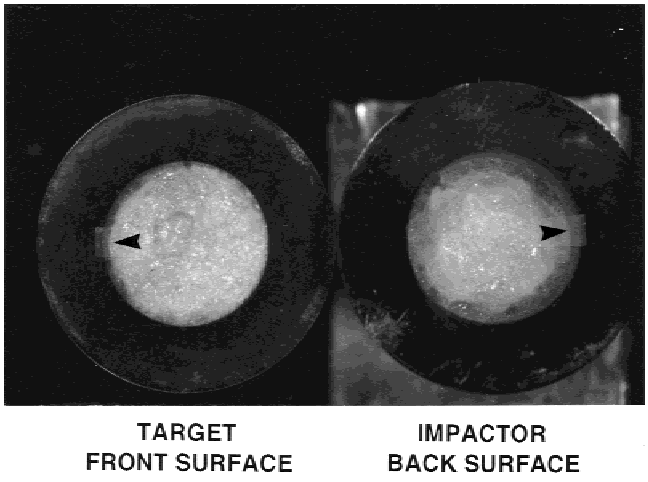

Fig. 14. Optical micrograph of recovered rods, experiment 4-1127. The arrows point to outer rings and split cracks.

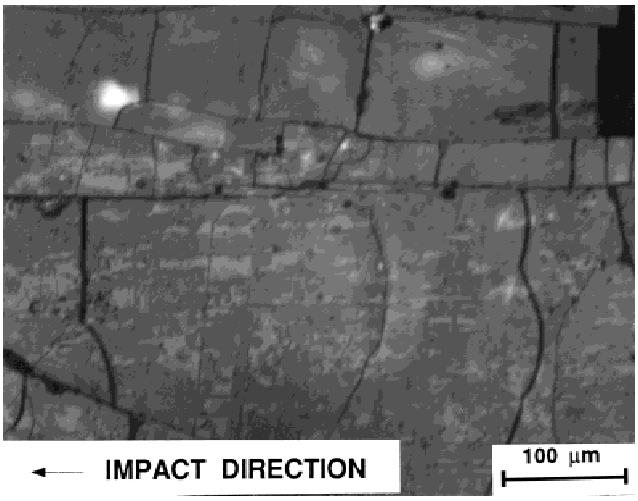

Fig. 15. Micrograph showing crack pattern on the outer surface of the recovered rods. Cracks in the direction of wave propagation and perpendicular to the bar axis are observed.

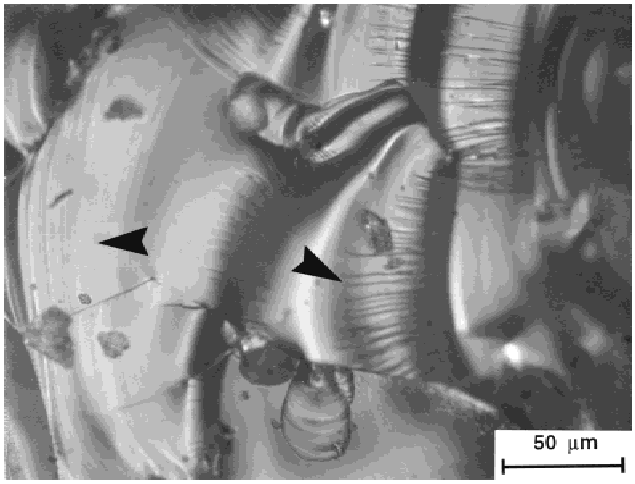

Fig. 16. Micrograph taken on the target-rod back surface showing typical features observed in glass fracture, i.e., hackles and Wallner lines.

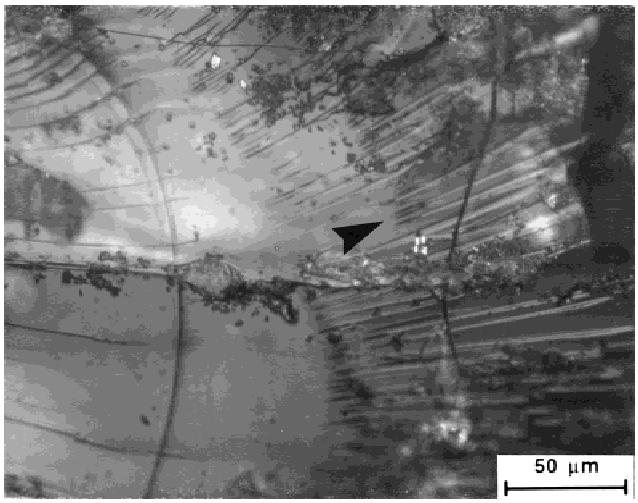

Fig. 17. Micrograph within the bar core showing twist hackles. Some hackles show discontinuity lines indicating crack propagation on other orientations *a posteriori* of the hackle formation.

of twist hackles, also known as shear hackles (Frechette[21]), cut by cracks on various orientations with and without twist hackles are seen in Fig. 17. Further evidence of the complexity of the fracture process is shown in Fig. 18. Primary and secondary twist hackles in the plane of the picture and perpendicular to it (see bottom), as well as Wallner lines are also identified in this region of the sample. A misted appearance, associated with high velocities of crack propagation, is shown in Figs. 19 and 20. A fibrous texture, generally elongated in the direction of cracking, is clearly observed in Fig. 20. It should be mentioned that this fibrous texture was observed only within the highly fractured core previously described. These micrographs reveal variable fragment sizes ranging from 50 to 150 μm.

X-ray analyses on recovered glass samples and intact glass were performed in order to investigate the possibility for crystallization hypothesized by Raiser and Clifton[12] and Clifton.[22] The X-ray experiments were conducted with an energy of characteristic radiation of 8.04 keV in copper targets, with a tube acceleration voltage of 40 kV, a step size of 0.05 degree and a count period of 6 s/degree. The results of these experiments are summarized in Fig. 21. X-ray diffraction patterns have been obtained from intact soda–lime glass samples, and shocked samples at two impact velocities (for details of the experimental configurations see Table I). We have performed X-ray measurements on glass powder taken from both the front and back of the recovered samples. In all cases a broad interference line is recorded characteristic of amorphous structures. The lack of distinct peaks in the diffraction pattern indicates the absence of crystallized glass at least in measurable volume fractions. We have also performed extended time detection measurements, with a count period of 11 min/degree, and obtained identical results. In shot 4-1008 the peak compressive stress was above the reported threshold for failure wave formation in plate experiments. Hence, these measurements do not provide evidence supporting phase transformation to a crystalline phase, one of the mechanisms discussed in Raiser and Clifton[12] and Clifton.[22] It should be emphasized that the absence of phase transformation in our confined rod experiments should be interpreted with caution because of the existence of a glass–steel interface in rod experiment which may lead to premature glass cracking at the rod periphery.

IV. Discussion and Concluding Remarks

In general, direct observation of the mechanisms leading to inelastic processes under dynamic loading is very difficult. Alternatively, indirect evidence of the material response is ob-

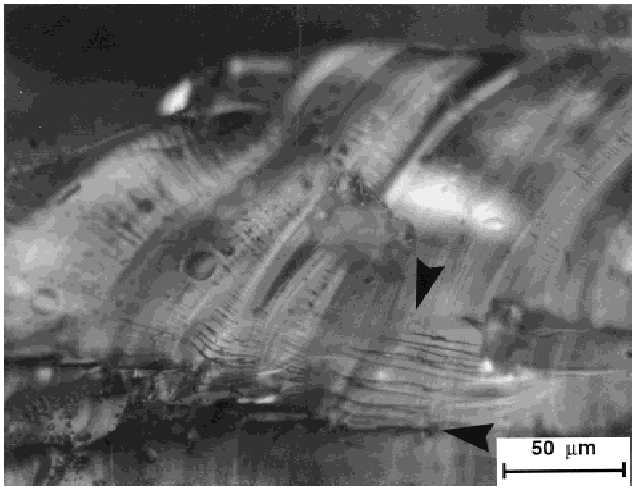

Fig. 18. Primary and secondary twist hackles in the plane of the crack and perpendicular to it. Wallner lines, probably resulting from the interaction of elastic waves emanating from other cracks fronts and the tip of the propagating crack in the plane of the picture, are observed.

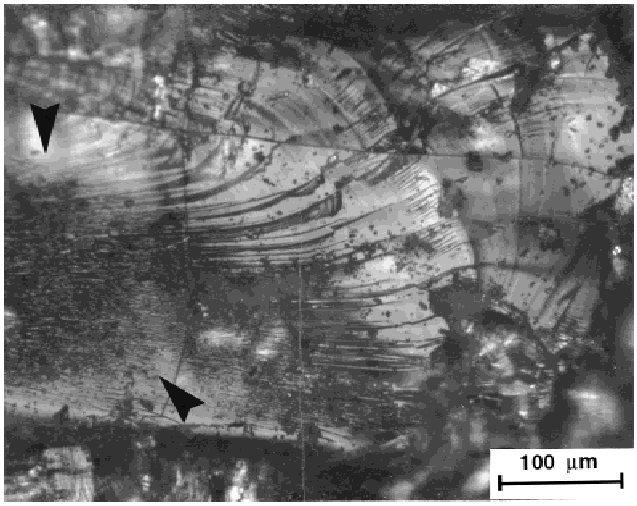

Fig. 19. Misted crack appearance resulting from high crack propagation speeds are seen.

tained from a variety of experimental configurations with different geometries and loading states. In this study we have reported experimental observations that provide a framework for the formulation of models that can capture the main features resulting from the so-called failure waves.

Based on the plate and rod experiments reported in this paper, we can make the following observations:

- Failure waves in plates (1-D strain) propagate from the specimen surface to the inside at a speed between 1.5 and 2 mm/μs. No significant incubation time is monitored in lateral gauge experiments.
- A threshold longitudinal stress of approximately 4GPa is required for the formation of failure waves in soda–lime glass and Corning 1723 glass.
- A dramatic reduction in spall strength is measured behind the failure wave front indicating that such wave is actually a moving boundary of damaged material.
- Lateral gauge experiments show that the shear resistance of the material behind the failure wave is drastically reduced. The residual shear strength is approximately the same as the one measured in high-strain-rate pressure-shear experiments by means of interferometric techniques. The latest experiments further indicate that the shear resistance is pressure dependent.
- Normal impact experiments, with embedded manganin gauges close to the impact surface, reveal the longitudinal stress progressively decays behind the failure wave front. This feature shows that the inelastic process responsible for the failure wave phenomenon has a well-defined kinetics.
- High-speed photography performed on unconfined glass rod experiments indicates the failure process initiates at the bar ends, impact and gauge planes, propagating toward the interior at a speed function of the peak compressive stress.
- Recovery experiments performed on confined glass rods reveal extensive fragmentation. Microscopy studies performed on the recovered samples show features commonly seen in glass fracture under tensile loading. It should be noted that these observations are performed after the material has been subjected to dynamic loading and unloading. Hence, knowledge of the fracture history is not available.
- X-ray experiments performed on the recovered glass bars show that the material retains its amorphous structure. This observation does not support glass crystallization as a possible explanation of the failure wave phenomenon.

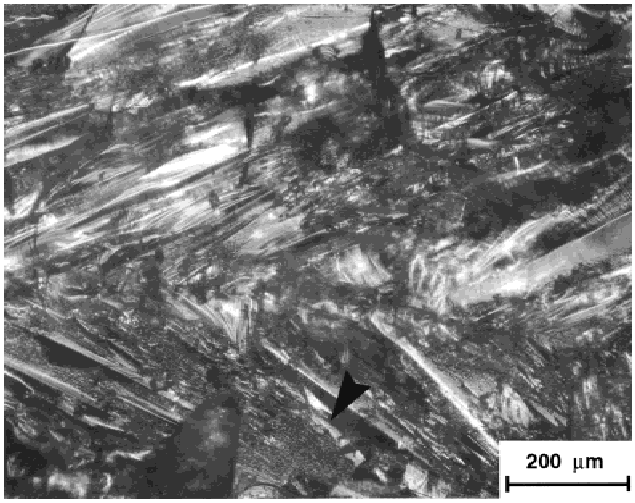

Fig. 20. Fibrous texture, generally elongated in the direction of crack propagation, is observed within the bar core.

Two interpretations of the failure process, consistent with the above features, are next examined. The first possibility is the initiation of microcracks at the glass surfaces being subjected to compressive tractions. Since the surface topography is far from being smooth on the atomic level, stress intensifications are always possible even on highly polished surfaces. Crack growth in a shear mode, following trajectories of maximum shear stress, may explain the generation of a moving boundary of damaged material. As pointed out by Raiser and Clifton,[12] a crack speed close to the Rayleigh wave speed results in a failure wave speed close to 2200 m/s, which is consistent with the experimental data. Although this mechanism can explain the increase in lateral stress and the lack of spall strength behind the failure wave, this mechanism appears to be inconsistent with the observed progressive spallation of glass behind the failure boundary.[12] Furthermore, the fractography presented in Section III does not unequivocally indicate crack propagation in mode II and/or mode III under a fully compressive stress state. The observed crack planes show features like twist and mist hackles which have been reported in the literature for dynamic crack propagation in mode I. It should be mentioned that confined rod experiments may present failure mechanisms that do not necessarily represent the failure mechanisms in plate impact experiments.

Another mechanism consistent with the failure wave observations and the inhomogeneous nature of plastic flow in amorphous materials at room temperature is the initiation of shear-

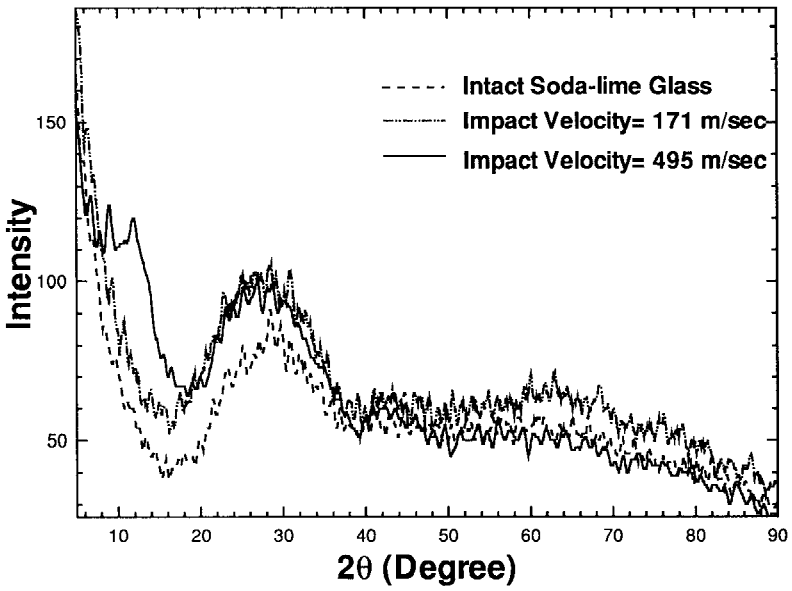

Fig. 21. X-ray diffraction diagram of soda–lime glass before and after impact loading.

induced flow planes in the specimen surfaces which are punched into the bulk of the material. Here again, surface stress intensification at the atomic level is invoked. These shear flow surfaces are driven predominantly by the deviatoric component of the stress tensor field. Small defects, voids or microcracks, nucleated at the intersection of these shear flow surfaces can subsequently grow under tensile loading resulting in a reduced but finite spall strength. It should be noted that the cohesive strength along shear-induced flow surfaces is generally reduced, leading to surfaces of weakness within the material and consequently a reduced tensile strength. The reader should keep in mind that an important difference between shear flow surfaces and microcracks is that in the case of shear flow surfaces the material preserves its cohesive strength, while in the case of cracks, the cohesive strength has been destroyed. Therefore, if a local tensile stress is applied, the response of glass containing shear flow surfaces will differ from the response of glass containing microcracks. This is basically the difference between plasticity and damage in micromechanics.

Although both mechanisms are consistent with the shear and spall strength changes observed behind failure waves, the shear-induced flow–microcracking mechanism is more in agreement with the fracture features observed in the recovered samples and the progressive spallation of glass behind the failure front. In fact, in the case of shear-induced flow, microcracking may occur at a later stage due to the accumulation of plastic deformation along flow planes or when the material is loaded in tension. Moreover, it can be envisioned that microcracks can propagate along shear flow surfaces, erasing features associated with plastic flow. Another feature of the shear-induced flow surface mechanism is that microcracks can be initiated within the specimen and not necessarily on the sample surface. This feature was observed experimentally by Senf *et al.*[23] in their work concerning visualization of fracture nucleation in impacted glass. Furthermore, the pressure dependence of the flow mechanism in amorphous materials may explain the suppression of the failure wave phenomenon at stress levels well above the HEL of the material (see Kanel *et al.*[2]). In fact, irreversible glass densification is expected to significantly increase the shear stress required for the formation of shear flow surfaces.

The observation that failure wave velocity in unconfined glass rods can approach the bar wave speed (see Fig. 12), which is in contrast with failure wave observations in plates (1-D strain), requires further discussion. In principle, this feature can be explained in terms of crack nucleation at the bar periphery upon the passage of the longitudinal pulse. Hence, differences in specimen geometry, between plate and rod experiments, affect not only the stress states but also the potential sites for crack nucleation from surface defects. Evidence of split crack formation due to radial expansion can be seen in Fig. 10 (see arrow in frame 7). These observations indicate care must be exercised in the interpretation of material failure under different loading and geometrical conditions. It is likely that the dominant failure mechanism in unconfined rods is not the same as the one present in confined rods or plate experiments.

Finally, we would like to mention that the experimental observations reported in this paper have important implications not only in the interpretation and modeling of dynamic failure in glass, but also in the identification of damage and inelasticity in ceramics, ceramic composites, and glass fiber composite materials. In the case of ceramics, it is well known that most commercial ceramics, Al_2O_3, SiN_4, TiB_2, and AlN, contain sintering aids in the form of glassy phases at grain junctions. It has been shown by Espinosa *et al.*[24] and Espinosa[25] that the existence of these second phases controls the dynamic resistance of these materials. Moreover, they have shown that grain boundary shearing acts as a precursor in the formation of microcracks along grain boundaries. This feature plays a very important role in modeling the kinetics of the failure process in these brittle materials. Similarly, glass failure under dynamic compression is expected to have important implications in the high strain rate response of glass fiber reinforced polymers and other composites. Fiber breakage in an S-2 glass woven composite has been investigated by Espinosa *et al.*[26]

Acknowledgments: H. D. Espinosa wishes to thank A. F. Grant and J. P. Sullivan for the encouragement and support provided during the development of the Dynamic Inelasticity Laboratory at Purdue University. The assistance of B. Sanders, D. Bower, J. Le, D. Reagan, W. Bader, M. Chadwell, and J. Zachary in the manufacturing of the light-gas gun is gratefully acknowledged.

References

[1]J. Cagnoux and F. Longy, ''Spallation and Shock-Wave Behavior of Some Ceramics,'' *J. Phys.* (*Paris*), **49,** C3–3 (1988).

[2]G. I. Kanel, S. V. Rasorenov, and V. E. Fortov, ''The Failure Waves and Spallations in Homogeneous Brittle Materials''; presented at the APS Topical Conference on Shock Compression of Condensed Matter (Williamsburg, VA, 1991).

[3]Z. Rosenberg, D. Yaziv, and S. J. Bless, ''Spall Strength of Shock-Loaded Glass,'' *J. Appl. Phys.,* **58,** 3249 (1985).

[4]N. S. Brar and S. J. Bless, ''Failure Waves in Glass under Dynamic Compression,'' *High Press. Res.* **10,** 773–84 (1992).

[5]F. Spaepen, ''A Microscopic Mechanism for Steady State Inhomogeneous Flow in Metallic Glasses,'' *Acta Metall.,* **25,** 407–15 (1977).

[6]A. S. Argon, ''Plastic Deformation in Metallic Glasses,'' *Acta Metall.,* **27,** 47–58 (1979).

[7]P. S. Steif, F. Spaepen, and J. W. Hutchinson, ''Strain Localization in Amorphous Metals,'' *Acta Metall.,* **30,** 447–55 (1982).

[8]H. D. Espinosa and N. S. Brar, ''Micromechanical Study of Inelasticity in Brittle and Amorphous Materials,'' proposal submitted to the Army Research Office, Research Triangle Park, NC, 1992.

[9]D. M. Marsh, ''Plastic Flow in Glass,'' *Proc. R. Soc. London, A,* **279,** 420 (1963).

[10]J. T. Hagan, ''Shear Deformation under Pyramidal Indentation in Soda–Lime Glass,'' *J. Mater. Sci.,* **15,** 1417 (1980).

[11]B. R. Lawn, T. P. Dabbs, and C. J. Fairbanks, ''Kinetics of Shear-Activated Indentation Crack Initiation in Soda–Lime Glass,'' *J. Mater. Sci.,* **18,** 2785–97 (1983).

[12]G. Raiser and R. J. Clifton, ''Failure Waves in Uniaxial Compression of an Aluminosilicate Glass''; pp. 1039–42 *High Pressure Science and Technology.* Edited by S. C. Schmidt. Joint AIRAPT–APS Conference, Colorado Springs, CO, 1994.

[13]G. I. Kanel, A. M. Molodets, and A. N. Dremin, ''Investigation of Singularities of Glass Strain under Intense Compression Waves,'' translated from *Fizika Goreniya i Vzryva,* **13** [6] 906–12 (1977).

[14]M. K. W. Wong and Y. M. Gupta, ''Dynamic Inclusion Analyses of Lateral Piezoresistance Gauges under Shock Wave Loading''; pp. 871–74 in *Shock Compression of Condensed Matter, 1991.* Edited by S. C. Schmidt, R. D. Dick, J. W. Forbes, and D. J. Tasker. Elsevier, Essex, U.K., 1991.

[15]Z. Rosenberg and N. S. Brar, ''Hysteresis of Lateral Piezoresistive Gauges''; pp. 1707–10 in *High Pressure Science and Technology.* Edited by S. C. Schmidt. Joint AIRAPT-APS Conference, Colorado Springs, CO, 1994.

[16]H. D. Espinosa and R. J. Clifton, ''An Experimental Investigation of Inelasticity in Shock Loaded AlN/Al Composites''; pp. 37–56 in Proceedings of the Symposium on Experiments in Micromechanics of Fracture-Resistant Materials (ASME Winter Annual Meeting, Atlanta, GA), AMD-Vol. 130. Edited by K. S. Kim. American Society of Mechanical Engineers, New York, 1991.

[17]Z. Rosenberg and Y. Partom, ''Longitudinal Dynamic Stress Measurements with In-Material Piezoresistive Gauges,'' *J. Appl. Phys.,* **58,** 1814 (1985).

[18]H. D. Espinosa and N. S. Brar, ''Dynamic Failure Mechanisms of Ceramic Bars: Experiments and Numerical Simulations,'' *J. Mech. Phys. Solids,* **43** [10] 1615–38 (1995).

[19]P. Kumar and R. J. Clifton, ''Optical Alignment of Impact Faces for Plate Impact Experiments,'' *J. Appl. Phys.* **48,** 1366 (1977).

[20]D. P. Dandekar and P. A. Beaulieu, ''Failure Wave under Shock Wave Compression in Soda Lime Glass''; pp. 211–18 in *Metallurgical and Material Applications of Shock-Wave and High-Strain-Rate Phenomena.* Edited by L. E. Murr, K. P. Staudhammer, and M. A. Meyers. Elsevier, Amsterdam, Netherlands, 1995.

[21]V. D. Frechette (Ed.), Advances in Ceramics, Vol. 28, *Failure Analysis of Brittle Materials.* American Ceramic Society, Westerville, OH, 1990.

[22]R. J. Clifton, ''Analysis of Failure Waves in Glasses,'' *Appl. Mech. Rev.,* **46** [12] 540–46 (1993).

[23]H. Senf, E. Straßburger, and H. Rothenhäusler, ''Visualization of Fracture Nucleation during Impact of Glass''; pp. 163–70 in *Metallurgical and Material Applications of Shock-Wave and High-Strain-Rate Phenomena.* Edited by L. E. Murr, K. P. Staudhammer, and M. A. Meyers. Elsevier, Amsterdam, Netherlands, 1995.

[24]H. D. Espinosa, G. Raiser, R. J. Clifton, and M. Ortiz, ''Experimental Observations and Numerical Modeling of Inelasticity in Dynamically Loaded Ceramics,'' *J. Hard Mater.,* **3** [3–4] 285–313 (1992).

[25]H. D. Espinosa, ''Micromechanics of the Dynamic Response of Ceramics and Ceramic Composites''; Ph.D. Thesis. Brown University, Providence, RI, 1992.

[26]H. D. Espinosa, G. Emore, and Y. Xu, ''High Strain Rate Behavior of Composites with Continuous Fibers''; pp. 6–16 in *High Strain Rate Effects on Polymer, Metal and Ceramic Matrix Composites and Other Advanced Materials,* AD-Vol. 48. Edited by Y. D. S. Rajapakse and J. R. Vinson. American Society of Mechanical Engineers, New York, 1995. □